# Interaction of multiple steps in hybrid rocket engines: Experimental investigation

C. Glaser, J. Hijlkema, J.-Y. Lestrade, J. Anthoine

# Interaction of multiple steps in hybrid rocket engines: Experimental investigation

C. Glaser *, J. Hijlkema, J.-Y. Lestrade, J. Anthoine

*ONERA/DMPE, Université de Toulouse, F-31410 Mauzac, France*

ARTICLE INFO

*Keywords:*
Genetic algorithm
Multi-step fuel
Regression rate enhancement
Recirculation zone
Hybrid rocket engine

ABSTRACT

In this article, we investigate the interaction of multiple steps in hybrid rocket fuel grains. Previous studies have shown the potential of single steps to increase the regression rate. In this study, we evaluate if the single step results can be translated to a multi-step approach. Of special interest are the interactions between the different step configurations. Four grain profiles are assembled by using fuel grain segments with different inner diameters, therefore forming a multi-step approximation of the profiles that can easily be manufactured and scaled up. The multi-step grains enhance the regression rate because of increased mixing and convective heat transfer induced by the recirculation zones of the steps. The experimentally obtained regression rate profiles are similar to the single step experimental data. This signifies that they are reproducible and therefore predictable. Most importantly, multiple steps do not interfere negatively with each other, which proves that steps can be used to approximate different fuel grain profiles. We show experimentally that the regression rate can be increased up to 81% by accumulating the regression rate enhancing potential of single steps. Moreover, we developed a genetic algorithm to estimate the spatially resolved Marxman parameters with only one single burn.

## 1. Introduction

The versatility of Hybrid Rocket Engines (HREs) in terms of propellant choice, throttleability and overall application is well known [1–3]. However, challenges like low regression rates, high fuel residuals, Oxidizer-to-fuel (O/F) ratio shift and the overall inferior maturity of HREs are limiting the widespread utilization of HREs in the space domain [4–6]. In previous work [7,8], we proposed a novel approach to tackle low regression rates, and possibly O/F shift and residuals in one design. Additionally, this proposed stepped design approach can potentially increase the overall versatility of HREs because it allows tailoring the engines' performance exactly to the envisioned use-case. The concept is to use multiple fuel grain segments rather than one single grain. The fuel grain segments can have different inner diameters (or any other desired geometric characteristic) to form a fuel grain geometry that is approximated by steps. Due to the steps, mixing and convective heat transfer increase due to the formation of recirculation zones [7,9,10]. As a consequence, the regression rate is augmented. The multi-step concept enables advanced geometries (even helical designs [11]) that otherwise would need to be printed, which can limit fuel choice, density control and large-scale applications, although the field of additive manufacturing in HREs is expanding [12–15].

Our previous work concentrated on the numerical and experimental investigation of a single step inside the engine. Both backward- (BFS) and forward facing steps (FFS) have been assessed. Experimentally [7] and numerically [8], the regression rate increased locally due to the enhanced mixing and convective heat transfer. Moreover, an important length-to-height relationship of the zone of influence of steps was derived. This work therefore is a direct continuation of previous efforts, and preliminary results have been presented in Ref. [16].

In the present article, we assess whether the observations of single steps are transferable onto multi-step profiles. The main objective of this work is to investigate the step-step interactions and whether they differ from the behavior of single steps. Open literature on multi-step regression rates is lacking in-depth investigation on the continuous regression rate profiles or correlation with no-step cases, let alone comparison between single- and multi-step grains (see Section 2). Instead of randomly distributing steps, we propose to distribute multiple steps to follow different fuel grain geometries.

Additionally, we present a genetic algorithm [17,18] that allows estimating the spatially resolved Marxman fit in the form of: [19]

$$\dot{r} = a \cdot G^n \cdot x^b \,, \tag{1}$$

where $\dot{r}$ is the time-averaged regression rate, $G$ the total mass flux, $x$ the axial coordinate and $a, b, n$ empirical Marxman parameters that best fit

* Correspondence to: German Aerospace Center (DLR), Eugen-Sänger-Str. 50, 29328 Faßberg, Germany.

**Nomenclature**

**Greek symbols**

| | |
|---|---|
| $\epsilon$ | Error |
| $\eta_{c*}$ | c* combustion efficiency |
| $\rho_f$ | Fuel density |

**Symbols**

| | |
|---|---|
| $a$ | Marxman parameter |
| $A_{i,j}$ | Port area at index $i, j$ |
| $b$ | Marxman parameter |
| $N$ | Total number of axial discretization steps |
| $c^*$ | Characteristic velocity |
| $D_{\text{avg}}$ | Average port diameter during burn |
| $D_{\text{exp}}$ | Final experimental diameter |
| $D_f$ | Final port diameter |
| $D_{i,j}$ | Port diameter at index $i, j$ |
| $D_{\text{num}}$ | Final numerical diameter |
| $D_m$ | Motor diameter |
| $D_0$ | Initial port diameter |
| $G$ | Mass flux |
| $G_{\text{ox}}$ | Oxidizer mass flux |
| $g$ | Acceleration of gravity |
| $I$ | Individual |
| $I_{\text{sp}}$ | Specific impulse |
| $L$ | Fuel port length |
| $L_g$ | Fuel grain length |
| $M$ | Number of random individuals |
| $\Delta m_f$ | Fuel mass loss |
| $\dot{m}_{\text{fuel}}$ | Fuel mass flow |
| $\dot{m}_{i,j}$ | Total mass flow at index $i, j$ |
| $\dot{m}_{\text{ox}}$ | Oxidizer mass flow |
| $n$ | Marxman parameter |
| $n_{\text{best}}$ | Number of best individuals |
| O/F | Oxidizer-to-fuel ratio |
| $P$ | Population |
| $P_c$ | Chamber pressure |
| $Q$ | Quality criterion |
| $\dot{r}$ | Regression rate |
| $\dot{r}_{\text{ref,marx}}$ | Constructed Marxman reference case |
| $S$ | Total number of segments |
| $S_{i,j}$ | Burning surface at index $i, j$ |
| $T$ | Thrust, total number of time steps |
| $t_b$ | Burn time |
| $x$ | Axial coordinate |
| $x/h$ | Length-to-height ratio |

the experiments. Usually, to obtain the empirical Marxman parameters, multiple experiments need to be performed. With the genetic algorithm, a single test firing can suffice.

The article is structured as follows: first, literature relevant to our case is presented. Then, the genetic algorithm to obtain the Marxman parameters is explained. Finally, four profiles are approximated by steps and the experimental results discussed.

## 2. Stepped designs in the literature

Numerous designs to increase the regression rate can be found in the HRE literature [20,21], however, the literature on steps in hybrids is limited. Korting et al. [22] tested a BFS at the inlet of their hybrid motor. Locally, the regression rate doubled compared to the reference cases due to the formation of a recirculation zone. In fact, the highest regression rate could be traced back to the point of the re-attachment of the flow after the recirculation zone. Moreover, Korting et al. [22] tested different oxidizer mixtures (ranging from 100% pure oxygen to 20% oxygen with 80% nitrogen). Interestingly, for mixtures with 20% oxygen, combustion only occurred when the stepped design was used. In a reference case without step and 20% oxygen, the motor would not ignite. The explanation for this phenomenon lies in the increased mixing due to the recirculation zone after the step. For low oxygen environments, the base-line mixing of the reference cases was not enough to promote ignition.

Kamps et al. [23] included a BFS in the middle of their motor (10 mm height) to augment mixing. Directly after the step, the regression rate decreased shortly (inside the recirculation zone length) to then display a local maximum in regression rate. Lee et al. [24] investigated the use of a BFS (5–7.5 mm height), to not only increase the regression rate, but also to decrease the pressure oscillations compared to a diaphragm case. The stepped design increased the average regression rate downstream the step by up to 50% and decreased the pressure oscillations down to 4% of the mean chamber pressure. Musa et al. [25] researched numerically the use of BFS and FFS in a Solid Fuel Ramjet (SFRJ) that uses High-Density Polyethylene (HDPE). Apart from the oxidizer (which is air), SFRJs have the same cylindrical combustion chambers as HREs. For this reason, they can be compared to the hybrid engine combustion. Musa et al. [25] stated that in the case of BFS, the regression rate directly after the step decreases drastically inside the recirculation zone to then increase considerably after the re-attachment. For FFS, the decrease in regression rate is already visible before the step, as the flame is pushed away from the fuel surface. After the step, the regression rate is higher than before (because of the difference in mass flux), with a distinct local peak in regression rate which is attained further upstream than for a BFS case.

We were able to show the effect of steps experimentally [7] and numerically [8] in previous research of a single BFS and FFS (7.5 mm each). For proper comparison, we added different reference cases to quantify the effect for each mass flux. Directly after the BFS, the local regression rate decreases below the reference because of the flame being further away from the fuel surface and the recirculation zone hindering the boundary layer to be fully developed. After the re-attachment, the regression rate increased by a constant value over the reference cases, leading to a total increase in the space- and time-averaged regression rates of around 20% for the BFS case for total fuel grain lengths of 500 mm and 16% on a motor with 110 mm length. For the FFS cases, the regression rate decreases already before the step and shows a local maximum directly after the step, which is reached further upstream than for the BFS cases. Quantitatively speaking, for a total grain length of 500 mm, the space- and time-averaged regression rate did not increase because the local maximum is too thin to be noticeable on a long grain. On the motor with the short grain (110 mm), however, the average regression rate increased by around 40%. The reason for this behavior was found in the total fuel grain length [7]. The BFS cases have a constant increase in regression rate after the step, whereas the FFS case are more pronounced but limited in their area of influence. As a first postulation, when it comes to distributing multiple steps along a profile, FFS should be placed close to each other to prolong their area of influence whereas BFS should be given space in between them to profit from the constantly increased regression rates.

The distribution of multiple steps has been researched by Sakashi et al. [26] with a set of BFS and FFS (called concave–convex design) and heights between 3 to 9 mm. The average regression rates increased by up to 100%. The step heights were more important than the step width. Interestingly, for increasing step height, the c* efficiency declined. From 96% with a step height of 3 mm to 92% with 6 mm step height and 91% for 9 mm step height. The positive effects of the steps

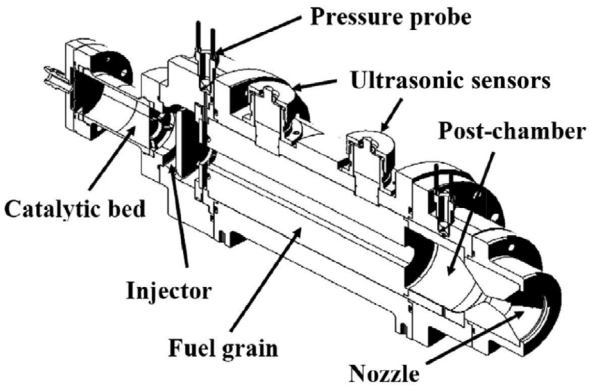


**Fig. 1.** Schematic of HYCAT.

were visible both with and without swirling injection, hinting at the possibility to combine both approaches to increase the regression rate. Kumar and Joshi [27] investigated a grain with a sequence of four alternating BFS/FFS. The average regression rate increased up to 55%, well in line with the aforementioned literature.

A noteworthy similar method to increase regression rates of HREs by up to 90% through mixing and increased turbulence are diaphragms inside the fuel grain, either with single [28–31], or multiple distributed diaphragms [32,33].

## 3. Experimental methods

This section gives a short overview of the experimental equipment and methods used to obtain experimental results.

### 3.1. HYCAT test facilities

The HRE used in this study is the HYCAT (*Hybrid with CATalyzer* [34]) engine of ONERA. The schematic of HYCAT is shown in Fig. 1. It uses hydrogen peroxide ($H_2O_2$) in an 87.5% concentration as oxidizer and HDPE as fuel. The hydrogen peroxide is decomposed over a catalyst and the hot decomposition products ignite the engine before the combustion gases are expanded through an ablatively cooled graphite nozzle. The temperature upstream of the injector is measured, which was held similar throughout all presented tests. A Coriolis mass-flow meter measures the oxidizer mass flow rate, and the chamber pressure is obtained in the pre- and post-chamber by four piezoelectric pressure probes. In all our test cases, a simple axial injector is used. The total length of the fuel grain is 500 mm. The thrust is measured in x, $y$ and z directions. Tests conducted on the HYCAT engine are abbreviated with the letter $H$ followed by the number of the test, e.g., H48.

### 3.2. Mass loss method

Probably the most common method to estimate the time- and space-average regression rate is the mass loss method. The fuel grain is weighed before and after the test. With the known mass loss and assuming uniform and cylindrical consumption, the final diameter of the fuel grain can be estimated as [35]:

$$D_f^2 = \frac{4\Delta m_f}{\pi \rho_f L_g} + D_0^2 \,. \tag{2}$$

Knowing the final diameter ($D_f$) and the initial diameter ($D_0$), the regression rate (averaged in space and time) can be calculated using the burn time ($t_b$):

$$\dot{r} = \frac{D_f - D_0}{2t_b} \,. \tag{3}$$

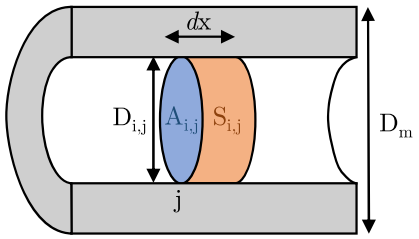


**Fig. 2.** Discretization of fuel grain at time $i$.

### 3.3. Longitudinal slicing

Another method to obtain also the local regression rate profiles was presented in Ref. [7]. The principle is to cut the fuel grains after the tests along their longitudinal axis. With a standard office scanner and an image processing software such as *Fiji* [36], the local final diameter $D_f(x)$ can be obtained. The time averaged local regression rate (assuming axisymmetry) denotes therefore to:

$$\dot{r}(x) = \frac{D_f(x) - D_0(x)}{2t_b} \,. \tag{4}$$

## 4. The genetic algorithm

The principle of the genetic algorithm [18] can be described in a single sentence: create an initial population $P_0$ with $M$ random individuals $I$, select the best individuals, cross-breed and mutate them and repeat from the beginning. The algorithm is an adapted and improved version of the genetic algorithm presented in Ref. [18]. The genetic algorithm can be used to obtain the empiric Marxman parameters $a, b, n$ (Eq. (1)) with a single test. In the respective subsections, we elaborate on the process.

### 4.1. Description of the genetic algorithm

The algorithm can be used to obtain the spatially resolved Marxman law, which is written in Eq. (1), with a single test firing. Usually, multiple tests at different diameters and mass fluxes need to be conducted to get an estimate of the Marxman law, and even then, it is often not possible to estimate the axial component ($x^b$). With our adapted genetic algorithm, a single test suffices.

The Individuals $I$ of the population $P$ in this adaption are defined by the empirical Marxman parameters $a, b, n$:

$$I = [a, b, n]. \tag{5}$$

The initial profile always starts at the initial port diameter ($D_0$) that corresponds to the test firing. To initialize the population $P_0$ (consisting of a set of individuals), a number of random individuals $I$ are generated. Next, for each individual of the population, the profile is regressed to judge its performance at the end of the simulated burn. The simulation is a simplified iterative simulation, where the time ($dt$, index $i$, total number of time steps $T$) and 1-D space ($dx$, index $j$, total number of axial steps $N$) are discretized (as depicted in Fig. 2) [18]:

$$S_{i,j} = \pi D_{i,j} dx \tag{6}$$

for the burning surface $S_{i,j}$. The fuel port Area $A_{i,j}$ can be described as:

$$A_{i,j} = 0.25\pi D_{i,j}^2 \,. \tag{7}$$

The total mass flow (oxidizer and fuel) denotes to:

$$\dot{m}_{i,j} = \dot{m}_{ox} + \sum_{j=1}^{j-1} \rho_f \dot{r}_{i,j} S_{i,j} \,. \tag{8}$$

The local regression rate is calculated using the known Marxman approach, taking into account also the axial distance $x = j * dx$:

$$\dot{r}_{i,j} = \begin{cases} a \cdot \left( \frac{\dot{m}_{i,j}}{A_{i-1,j}} \right)^n \cdot x^b & \text{if } D_{i,j} < D_m \\ 0 & \text{if } D_{i,j} \geq D_m \,, \end{cases} \tag{9}$$

which means that the algorithm stops regressing at point $j$ at time $i$ once the diameter of the motor $D_m$ is reached. The new fuel port diameter $D_{i+1,j}$ at station $j$ and time $i$+1 is updated as:

$$D_{i+1,j} = D_{i,j} + 2\,\dot{r}_{i,j}\,dt\,. \tag{10}$$

Finally, the average O/F ratio at time $i$ is determined as:

$$OF_i = \frac{\dot{m}_{\text{ox}}}{\dot{m}_{\text{fuel}}} = \frac{\dot{m}_{ox}}{\sum_{j=0}^{N} \rho_f \dot{r}_{i,j} S_{i,j}}\,. \tag{11}$$

After $T$ time steps (same as the experimental duration), the numerically obtained final diameters are compared to the final fuel port diameter obtained after the experiments $D_{\text{exp}}$ with the cutting method (see Section 3.3).

The quality criterion at any station j is defined as:

$$Q_{i=T,j} = \left| \frac{D_{\text{exp},i=T,j} - D_{i=T,j}}{D_{\text{exp},i=T,j}} \right| \tag{12}$$

and the average error denotes to:

$$\overline{Q} = \frac{\sum_0^N Q_j}{N}\,. \tag{13}$$

The population can now be sorted according to its quality.

At this point, the reproductive step of the genetic algorithm to construct a new generation $P_1$ is started:

1. Keep a number ($n_{\text{best}}$) of best individuals $I$.
2. Cross-breed the best individuals for all $n_{\text{best}}$.
3. Mutate the best individuals for all $n_{\text{best}}$.
4. Fill the rest of the population with random individuals.

The random cross-breeding and mutation operators can be found in Ref. [18].

The newly generated population $P_1$ can now be regressed again following the Eqs. (6)–(11), therefore closing the loop. The process is depicted in Fig. 3. It is considered finished when either a predefined minimum quality is attained or the maximum number of iterations is reached. Given the nature of genetic algorithms, there is no unique solution [18], but multiple semi-optimized solutions. Based on previous experiences documented in Ref. [18], the algorithm increases the quality of the population quickly for the first 1000 iterations. However, for additional iterations (even up to one million iterations), the quality does not increase significantly any more. This is why we chose 10 000 as a maximum number of iterations to save computational effort.

#### 4.1.1. Validation of the algorithm in marxman mode

To validate the approach to obtain the Marxman empirical parameters, we are testing it on two reference tests (H48 and H49, see Table 2) that we conducted in the past. Using the longitudinal slicing method presented in Section 3.3, the final diameter along the fuel grain axis is obtained. Moreover, the tests were conducted at different initial fuel port diameters (25 mm and 40 mm), which allows us to assess whether the Marxman empirical constants are valid for a larger range of fuel port diameters and mass fluxes.

Feeding the algorithm both final experimental profiles (H48 and H49) to search for the best fitting $a, b, n$ values of the Marxman law for both cases, the results after 10 000 iterations yield the following values (for regression rate in m/s, $G$ in kg/m$^2$s and $x$ in m):

$$\dot{r} = 9.03 * 10^{-7} \cdot G^{1.091} \cdot x^{-0.154} \tag{14}$$

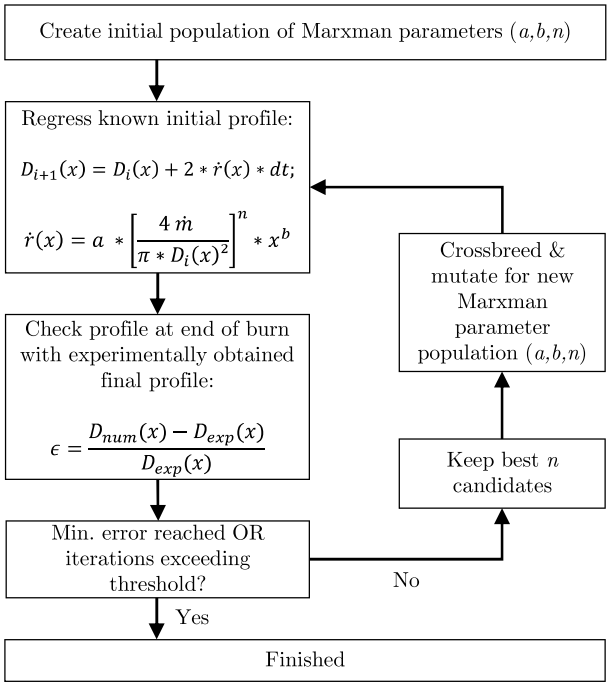


**Fig. 3.** The flow of the genetic algorithm to obtain Marxman parameters.

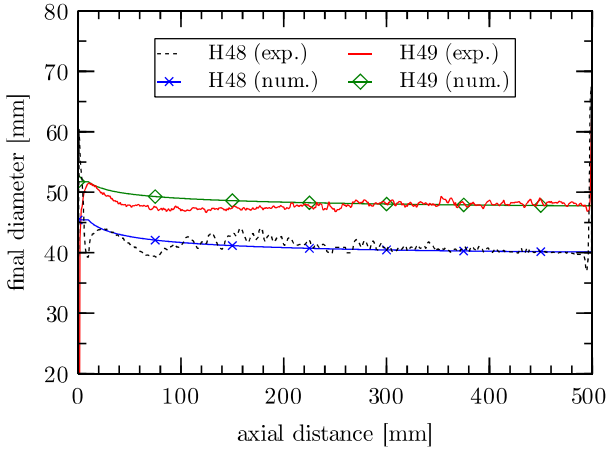


**Fig. 4.** Comparison of experimental final diameters and final diameters obtained with the Marxman empirical parameters obtained from two tests.

When these $a, b, n$ values are applied to the simulations of H48 and H49, the average relative discrepancy between the final diameter of the experiment and the algorithm is 1.8% in the case of H48 and 1.7% with H49. These results are displayed in Fig. 4 and show a good fit over the total fuel grain length, with larger discrepancies near the injector head.

To validate whether a single test firing can be used to predict also the final diameter of another test with reasonable accuracy, the approach is the following. The genetic algorithm calculates the Marxman parameters from either H48 ($D_0$ = 25 mm; $\dot{m}_{\text{ox}}$ = 0.337 kg/s) or H49 ($D_0$ = 40 mm; $\dot{m}_{\text{ox}}$ = 0.348 kg/s). Then, the Marxman parameters of H48 are applied to predict the final diameter of H49 numerically, and vice versa. The results are displayed in Fig. 5 and the Marxman parameters are given in Table 1. Looking at Table 1, the exponent $b$ of the axial distance $x$ remains almost constant. The empirical parameter $n$, however, decreases when using H49 instead of H48 to determine the Marxman parameters. This indicates that the genetic algorithm finds a higher mass flux dependency in the test of H48 (high initial mass flux)

**Table 1**
Marxman parameters obtained by genetic algorithm. $\dot{r}$ in m/s, $G$ in kg/m$^2$s and $x$ in m.

| | a | n | b | $D_f$ error |
|---|---|---|---|---|
| Using H48 & H49 | $9.03*10^{-7}$ | 1.091 | −0.154 | 1.8% |
| Using only H48 | $4.98*10^{-6}$ | 0.827 | −0.090 | 4.4% |
| Using only H49 | $1.04*10^{-5}$ | 0.622 | −0.100 | 12.6% |

than H49 (low initial mass flux). However, it is reminded that a genetic algorithm cannot find one unique optimal solution but rather multiple semi-optimal solutions. For this reason, the aforementioned trend is to be regarded with caution.

The discrepancy between predicted values and experimental values in Fig. 5 are 12.6% in the case of using the parameters of H49 for H48 and 4.4% when using the parameters of H48 for H49. Given that these predictions are carried out using only a single test firing, the accuracy is reasonable. The predictions of H49 using the Marxman parameters from H48 are considerably more accurate (4.4%). This is because H48 has roughly double the regression rate than H49 (see also Table 2). Therefore, the relative error in measuring the final diameter of H48 is roughly 5% whereas the error for H49 is estimated as 10% (both are conservative estimations calculated in previous work [8]). It appears that this error carries over also to the estimation of the Marxman parameter. Thus, it is recommended, to use the genetic algorithm from the highest regressing test case available, if only *one* test firing is used to estimate the Marxman parameters. Nonetheless, with *two* test firings, the predictions of the final diameters is well below 2% (see Fig. 4), so whenever possible, at least two test firings are to be preferred.

## 5. Preparation of the profiles

In this section, we obtain and prepare the fuel port profiles for the experimental test campaign. The different profiles originate from previous work [16], in an attempt to optimize the profiles to minimize O/F shift and residuals using an alteration of the genetic algorithm. However, since the optimization of the profiles was inconclusive, the origin of the shape of the profiles to be approximated with steps is not discussed in this article, but can be found in Ref. [16]. In the current work, the fuel grain shapes are used to incentivize the application of multiple steps to approximate a profile that otherwise would need to be printed.

### 5.1. Definition of an alternating stepped case

The first task is to create a reference case for a multi-stepped profile. So far, we only considered classical cylindrical fuel grains or grains with a single step [7,8]. While this was important to understand the fundamental mechanisms of steps in hybrid rocket engines, there is no indication whether the results of single step investigations can be applied to multi-stepped profiles. Thus, based on conclusions from Ref. [7], we prepared a multi-stepped profile with alternating steps to create a multi-stepped reference to evaluate if other profiles lose some maximal regression rate enhancement due to the steps being forced to follow a profile.

The alternating step grain is designed as a sequence of FFS and BFS with a step height of 7.5 mm. Based on Refs. [7,8], the approach is as follows: the area of the injector effects (increased heat transfer due to recirculation zone [37]) in our HYCAT engine is noticeable up to 50 mm axial distance. This area increases the regression rate, and therefore we keep the first 50 mm of the grain unaltered. After the first 50 mm, a total of 7 alternating steps (4 BFS and 3 FFS) are employed. Following the rule of thumb developed in previous research [7,8], the length after a BFS should be longer than for an FFS because a BFS increases the regression rate after the step by a constant value over the reference, whereas FFS have a more pronounced but shorter area

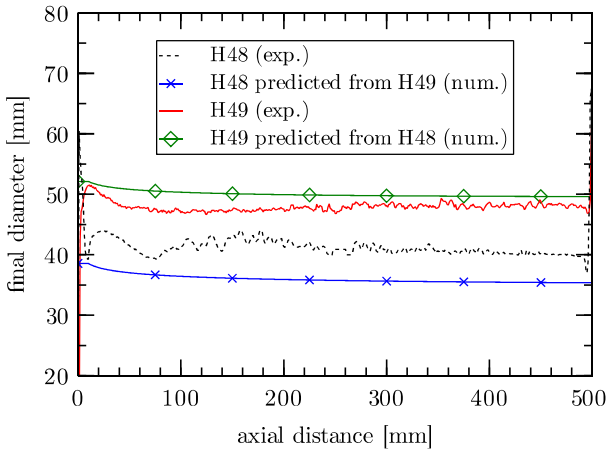


**Fig. 5.** Final diameters predicted with genetic algorithm using a single test.

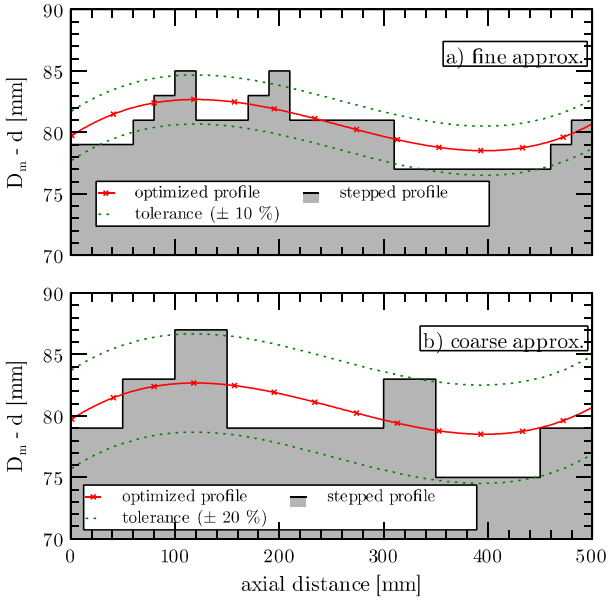


**Fig. 6.** Approximated profile. (a) fine approximation, (b) coarse approximation.

of influence. For this reason, a first alternating profile with a length-to-height ratio ($x/h$) of 10 for BFS and roughly 7 for FFS is decided upon. For a step height of 7.5 mm (to stay true to previous work on single steps) this translates to 75 mm length after the BFS and 50 mm after the FFS. Generally speaking, the alternating profile consists of grain segments with either 25 mm or 40 mm fuel port diameter.

### 5.2. Approximating fuel grain profiles with steps

Here, we present the different fuel grain profiles that are to be approximated with steps (see Fig. 6). To recall, the profiles originate from an attempt to optimize fuel grain profiles for a lower O/F shift [16]. Although the optimization was inconclusive, the shapes of the profiles are ideal candidates to investigate the distribution of steps along a profile. Theoretically, such profiles could be 3D-printed. However, this can limit fuel choice, density control and large-scale applications (for the current state of the art). Hence, in this section, we approximate the profile with steps (which represent fuel grain segments with different inner diameters). Based on our previous work on single steps (Refs. [7,8]), the approximation approach is the following:

**Table 2**
Summary of experimental data.

| Test | $\overline{D}_0$ [mm] | $t_b$ [s] | $\dot{m}_{ox}$ [kg/s] | O/F [–] | $G_{ox,avg}$ [kg/m²s] | $\dot{r}$ [mm/s] | $\Delta m_f$ [g] | $P_c$ [bar] | T [N] | $\eta_{c*}$ [%] | $I_{sp}$ [s] |
|---|---|---|---|---|---|---|---|---|---|---|---|
| H48 (Ref.) | 25.0 | 9.65 | 0.337 | 7.96 | 388.02 | 0.86 | 408.9 | 26.1 | 736.85 | 87.0 | 198.0 |
| H49 (Ref.) | 40.0 | 9.65 | 0.348 | 12.58 | 228.02 | 0.42 | 266.7 | 24.1 | 674.82 | 88.8 | 183.3 |
| H50 (single FFS) | 32.5 | 9.60 | 0.343 | 10.19 | 299.37 | 0.59 | 322.8 | 25.4 | 726.50 | 89.1 | 196.9 |
| H52 (single BFS) | 32.5 | 9.66 | 0.346 | 8.84 | 289.59 | 0.67 | 378.2 | 28.3 | 809.75 | 95.4 | 214.4 |
| H55 (alternating) | 34.0 | 9.44 | 0.326 | 6.66 | 241.52 | 0.79 | 462.2 | 27.9 | 802.68 | 94.3 | 218.2 |
| H56 (fine) | 40.1 | 9.51 | 0.337 | 9.59 | 211.46 | 0.52 | 334.2 | 25.9 | 742.59 | 90.6 | 203.4 |
| H57 (coarse)[a] | 40.4 | 9.60 | 0.344 | 8.83 | 208.36 | 0.57 | 374.4 | 26.8 | 796.89 | 89.6 | 212.0 |
| H60 (coarse) | 40.4 | 9.47 | 0.338 | 8.54 | 204.31 | 0.58 | 374.6 | 26.7 | 787.44 | 91.4 | 212.8 |
| Error estimation (conservative) | – | ±0.15 | $\pm 10^{-4}$ | ±0.1 | ±10 | ±0.02 | ±0.2 | ±0.01 | ±2 | ±0.1 | ±1.5 |

[a] The grain was inserted in the wrong orientation, see Section 6.3.

1. Apply two arbitrary tolerance levels (10% and 20%) to test the behavior of the approximation.
2. Keep the first 50 mm axial distance untouched for both cases to benefit from injector effects (increased regression due to recirculation zone [37]).
3. Distribute steps based on the rule of thumb from previous work [7,8]: larger distances and heights for BFS and more frequent steps for FFS
4. Follow two types of approximations: (i) fine approximation with step heights of 2 mm (FFS) and 4 mm (BFS), and (ii) coarser approximation with fixed six steps, step heights of 4 mm (FFS), and 8 mm (BFS).

Fig. 6 displays both profiles and the stepped approximation. For a more convenient interpretation of the curves, the diameters are the motor diameter $D_m$ (rounded to 100 mm) minus the inner diameter $d$. This way, the steps are illustrated the same way as they would be on a flat plane with steps, which is also indicated with the gray color under the curve, representing a fuel grain. In Fig. 6, the best practices to distribute steps become more visual. FFSs are followed by a next step considerably earlier than BFS.

## 6. Experimental results

All experimental data are obtained from the HYCAT facilities (see Section 3.1). Table 2 lists the experimental results of the tests, including error estimation. The error takes into account incertitudes of the sensors (oxidizer mass flow and pressure) and uncertainties of the total burn time on the HYCAT motor [34,38,39]. The highest error value of each group is applied to all tests. The high reproducibility of the HYCAT facilities has been already shown in Ref. [34].

Additionally, tests H48 and H49 are documented, which are cylindrical cases without steps. Moreover, for comparison, we added tests with single FFS (H50) and single BFS (H52) from our previous study [7,8].

The average mass flux is calculated using the average fuel port diameter throughout the burn, following the recommendation of Ref. [40]:

$$G_{ox,avg} = \frac{4\ \dot{m}_{ox}}{\pi\ D_{avg}^2}\ , \tag{15}$$

with the average port diameter during the burn denoting to:

$$D_{avg} = \frac{\overline{D}_0 + D_f}{2}. \tag{16}$$

The final diameter $D_f$ is obtained using the mass loss method (Section 3.2) of the total fuel grain mass loss to obtain an average representative final diameter. $\overline{D}_0$ is the average initial diameter. Since the multi-stepped fuel grains consist of different segments with different inner diameter and length, the average initial fuel grain diameter in these cases needs to be calculated using a weighted average:

$$\overline{D}_0 = \frac{\sum_1^S D_{0,i} * L_i}{\sum_1^S L_i}\ , \tag{17}$$

where $D_{0,i}$ is the fuel port diameter of the $i$th segment and $L_i$ the length of the $i$th segment and $S$ the total number of segments. The average regression rate ($\dot{r}$) is estimated using the mass loss method (Section 3.2). The specific impulse $I_{sp}$ is calculated as:

$$I_{sp} = \frac{T}{g\ (\dot{m}_{ox} + \dot{m}_{fuel})}\ , \tag{18}$$

with $g$ being the Earth's acceleration of gravity and the fuel mass flow $\dot{m}_{fuel}$ being calculated using the burn time $t_b$ and fuel mass loss $\Delta m_f$:

$$\dot{m}_{fuel} = \frac{\Delta m_f}{t_b}\ . \tag{19}$$

The results of the tests are discussed in detail in the following subsections.

### 6.1. Alternating profile of H55

Fig. 7 displays the experimental results of the alternating step profile (H55) in detail. The following elements are displayed in the illustration:

1. Local regression rate in Fig. 7(a)
2. Initial versus final diameter in Fig. 7(b). Note that the diameter displayed is the outer motor diameter ($D_m$) minus the inner diameter. This way, the profile can be interpreted as the lower half of the scan in Fig. 7(c).
3. Indication to distinguish between BFS and FFS for Fig. 7(a) and (b).
4. 2D Scan of fuel port geometry after the test in Fig. 7(c).

Since the alternating stepped profile consists of fuel grain segments of 25 mm and 40 mm, it is possible to compare them to the tests H48 ($D_0$ = 25 mm) and H49 ($D_0$ = 40 mm) with no steps. This is necessary because the regression rate of hybrids is strongly dependent on the fuel port diameter. The approach is depicted in Fig. 8, and the regression rate is calculated using the slicing method (Section 3.3).

Looking at the regression rate profiles of H55 in Fig. 7(a), the different effects of the BFS and FFS can be easily observed. For BFS, directly after the step, the regression rate drops below the reference case but increases shortly further downstream significantly over the reference regression rate. This is because directly after the step, the flame is further away from the fuel surface and, thus, the surface temperature is lower. With the surface temperature being a detrimental driver for the regression rate [7,8], the regression rate directly behind the BFS decreases. At the reattachment point of the flow, however, the regression rate increases and because of the augmented mixing and turbulence induced by the recirculation zone behind the step, the regression rate rises over the reference to a constantly higher level.

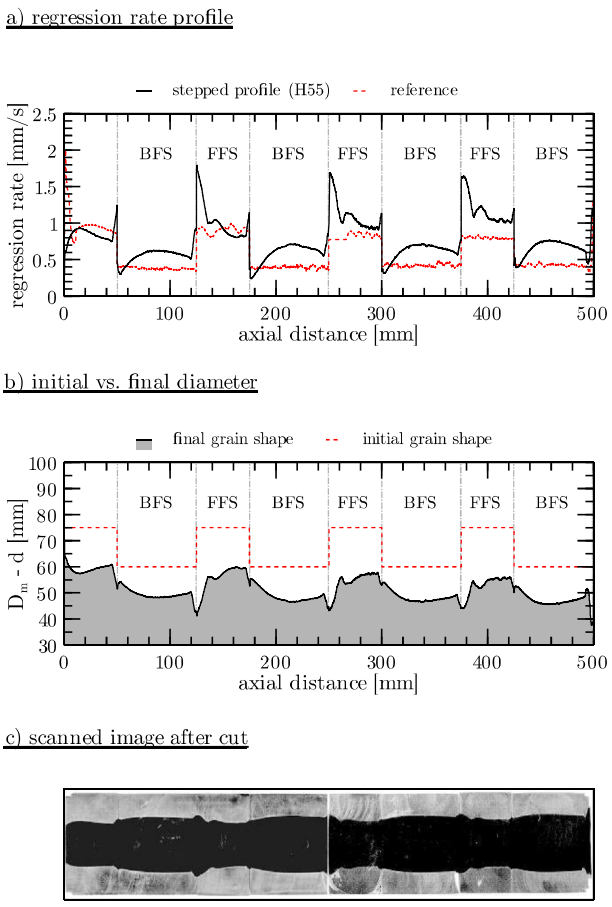


**Fig. 7.** H55 profiles (alternating steps).

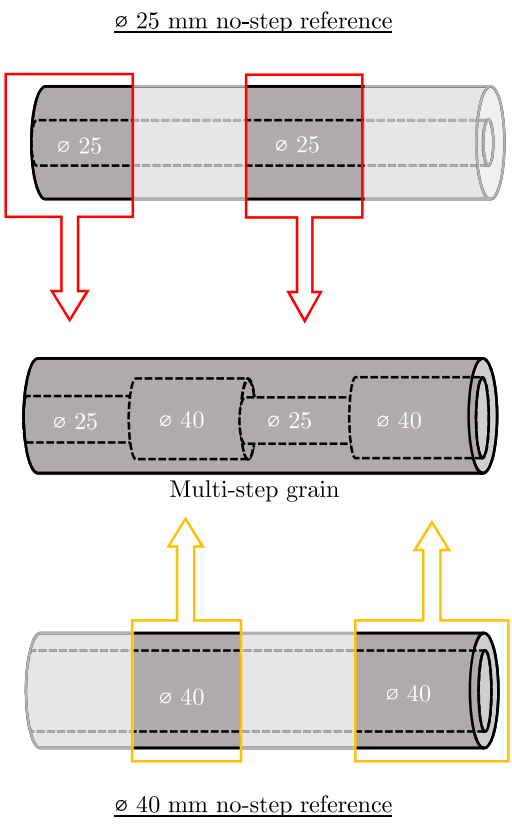


**Fig. 8.** Definition of reference cases.

For the FFS, the behavior is different: the FFS pushes the flame away from the surface already before the step, thus, decreasing the regression rate. After each FFS, two peaks in regression rate are visible. The first peak is due to the lateral progression of the FFS. Given the way the regression rate is calculated (final diameter minus initial diameter divided by the burn time), lateral fuel consumption (instead of radial regression) leads to these discontinuities. However, the second peak is the point of the reattachment of the flow and the increased mixing and turbulence shows itself in higher regression rates. Notably, the peak of the regression rate for FFS is considerably further upstream than in the case of BFS because for an FFS the diameter after the step is smaller and the flow accelerates.

We showed the aforementioned different effects of FFS and BFS on single stepped grains already numerically [8] and experimentally [7]. This signifies that the results of single step investigations can easily be translated to multi-step profiles. Moreover, in this work, we can investigate the interdependence of multiple steps for the first time. Three major observations are to be noted:

1. The shape of the regression rate profiles for BFS or FFS is very consistent throughout the profile, and it is unique to the type of step. The qualitative regression rate profiles are identical to the single step studies [7,8].
2. When an FFS follows a BFS, the regression rate drops already further upstream than for a single FFS.
3. The difference between the reference cases and the H55 profile increases further downstream. For the first 3 BFS, the H55 regression rate decreases for a short distance below the reference. At the last BFS, the regression rate still decreases directly after the step, however, it is constantly above the reference. The same is true for the FFS. While the regression rate of the first FFS drops below the reference cases, the other two FFS profiles are constantly above the reference. This proves that the regression rate increasing effects of steps can accumulate to considerably augment the average regression rate, rather than interfering negatively between each other. The higher regression rate also leads to a higher total mass flux, which could contribute to the increasing difference between reference cases and stepped case as well. This effect, however, is hard to quantify in the current study.

In Section 6.4, we will investigate the accumulation of average regression rates through multiple steps by consulting the time- and space-averaged regression rates of all multi-step profiles.

### 6.2. *Fine approximated profile*

In this section, we assess the profile which is closely approximated with small steps (2 mm for FFS and 4 mm for BFS, see also upper part of Fig. 6). Similar to the alternating profile of the previous section, in Fig. 9, the fuel grain scan after the test, the initial and final diameter as well as the regression rate profile is displayed.

For the multi-step cases (H56, H57 and H60), we cannot present experimental reference cases because the grain segments have a large variety of initial fuel port diameters. It would be necessary to conduct a no-step test at each diameter of the multi-step cases, which is resource intensive. Therefore, we developed so-called constructed Marxman reference cases. We obtained the Marxman parameters for the experimental no-step tests H48 and H49 (Fig. 13). The experimental final diameter of the *multi-step* tests (H56-H57 & H60) is known (either obtained from the mass loss or the slicing method, Section 3.2 and Section 3.3, respectively). Thus, a hypothetical *no-step* Marxman reference can be

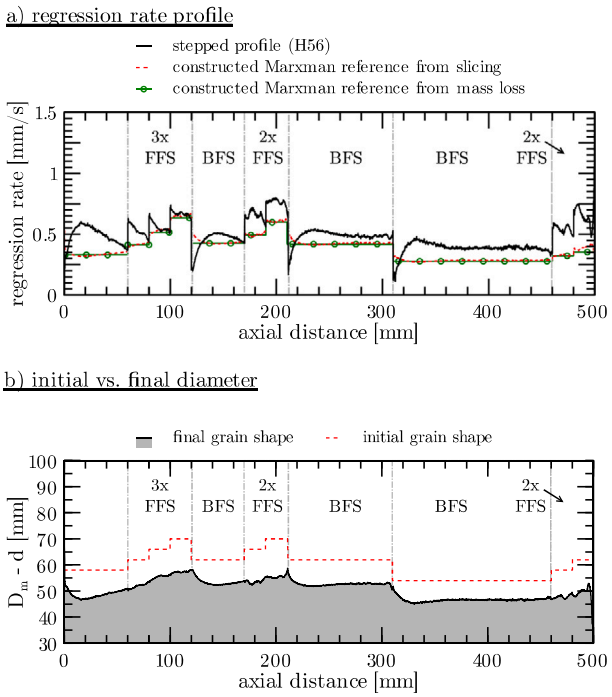


**Fig. 9.** H56 profiles (optimized profile, fine approximation).

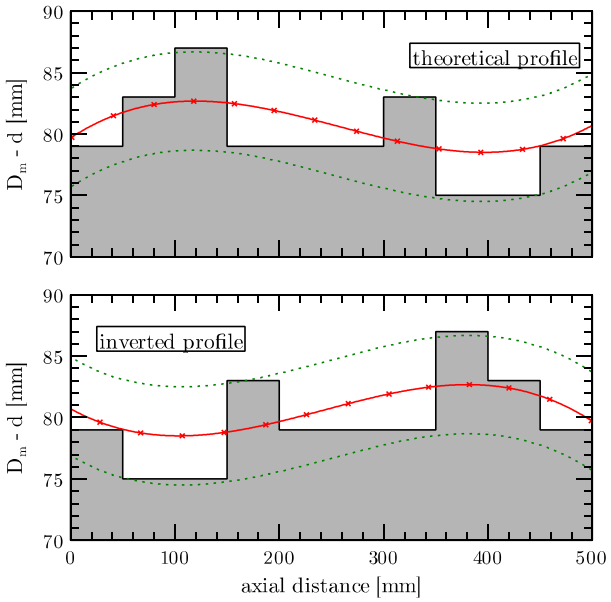


**Fig. 10.** Inverted profile of H57.

calculated using the experimental final diameters of the *multi-step* cases and using the Marxman parameters $(a, n)$ of the *no-step* cases:

$$\dot{r}_{\mathrm{ref,marx}} = a \cdot G_{\mathrm{ox}}^{n} = a \cdot \left[\frac{16\dot{m}_{\mathrm{ox}}}{\pi \cdot (D_0 + D_f)^2}\right]^{n} . \tag{20}$$

Eq. (20) does not take into account the local dependency $x^b$, because the Marxman parameters ($a = 0.0003$ and $n = 1.328$) of Eq. (20) are obtained experimentally using the measurable oxidizer mass flow and the mass loss method without the genetic algorithm. The final diameter $D_f$ is either obtained from the mass loss method (of each grain segment, therefore discrete) or the slicing method (continuous). While the constructed Marxman reference cases might not achieve the same precision as those from actual test firings (as depicted in Fig. 7a), they offer a scientific basis to evaluate the multi-step performance of any given fuel grain port diameter, without the need for further tests. Thus, Eq. (20) is applied in Figs. 9(a), 11(a) and 12(a).

Turning the attention to Fig. 9, the most prominent observation is that the profile that is visible in the scan of Fig. 9(c) is almost completely smooth, and the steps have vanished. Only the markings left by the recirculation zones show traces of the steps. This observation leads to the conclusion that the step heights of 2–4 mm are disappearing after at least 10 s burn time for our set-up. Consequently, with increasing burn time, the steps progress and the fuel port becomes smooth. Thus, we obtain a smooth profile that we wanted to approximate with steps.

Since H56 is approximated with 10 steps, we can investigate how multiple steps interact with each other. Looking at the regression rate profiles in Fig. 9(a), it is surprising how consistent the characteristic shapes of the BFS and FFS regression rate profiles are: for the FFS, the first peak (discontinuity to be more precise), which displays the lateral progression of the step, is visible, followed by a smaller peak that shows the increase in regression rate due to the recirculation zone. Especially looking at the first triple of FFS, the resemblance of the shape is surprising.

For the BFS, likewise, the shape of the regression rate is similar across all BFS. The decrease in regression rate directly after the step because of the flame being further away from the surface is followed by a considerable increase in regression. Additionally, it is visible that when an FFS follows on a BFS, the regression rate at the end of the BFS zone decreases because of the flame being pushed further away from the surface. For example, consider the shape of the regression rate profile of the first BFS and the second BFS. At the first BFS, the profile has a strongly concave shape (thus the regression rate decreases before the next FFS). For the second BFS, however, the regression rate profile is almost constant. The same effect was already visible in the alternating profile (Fig. 7).

Looking at the initial vs. final diameter in Fig. 9(b), it becomes clear that the steps completely disappeared within 10 s. It is therefore of interest, how the coarse profile with larger steps of H57 & H60 performs in the next section.

### 6.3. Coarse approximated profile

We present the test of the profile approximated with fewer but taller steps here. The total number of steps is 6 (close to the alternating profile H55) and the height varies between 4 mm and 8 mm. Unfortunately, during the assembly and preparation of the motor, we inserted the fuel grain the opposite way, meaning that the profile was inverted on the first test (H57). Fig. 10 shows the planned profile and compares it to the profile that was tested in reality because of the wrong preparation of the motor. This accident, however, gives us valuable data whether our defined rule of thumb is valid or not and how multiple steps interact with each other. The test with the correct grain orientation (H60) will be presented afterward. To recall, based on previous research on single steps, we postulated that BFS should be as tall as possible and spaced further from a next step. For FFS, the height should be limited, and they are preferably spaced close to a next step. By accidentally inverting the profile on H57, we can test this hypothesis because the inverted profile is now exactly opposite to what was desired: many small BFS (4 mm) followed by a few tall FFS (8 mm).

Fig. 11 displays the experimental data (scan, diameter, regression rate) of the inverted profile. Looking at the regression rate profile of

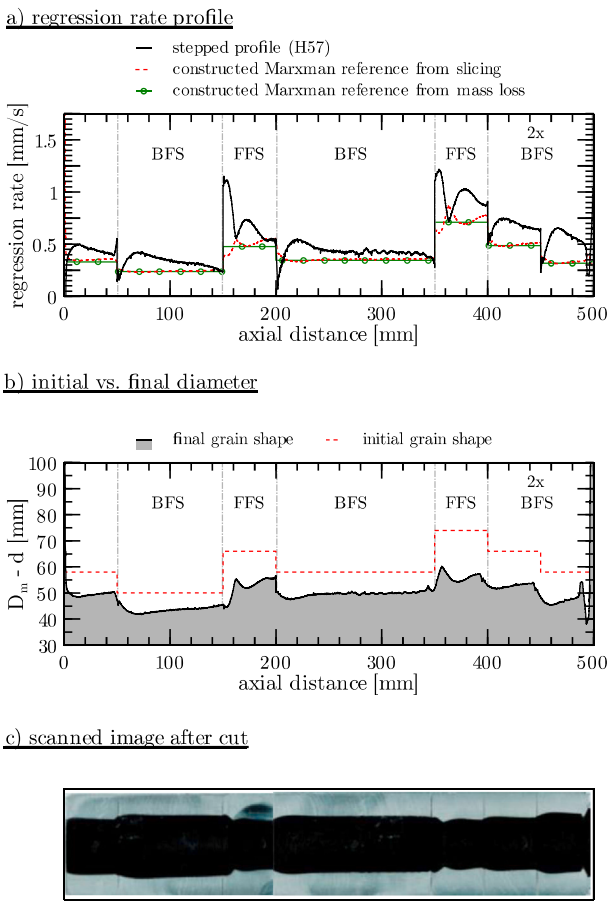


**Fig. 11.** H57 profiles (inverted profile, coarse approximation).

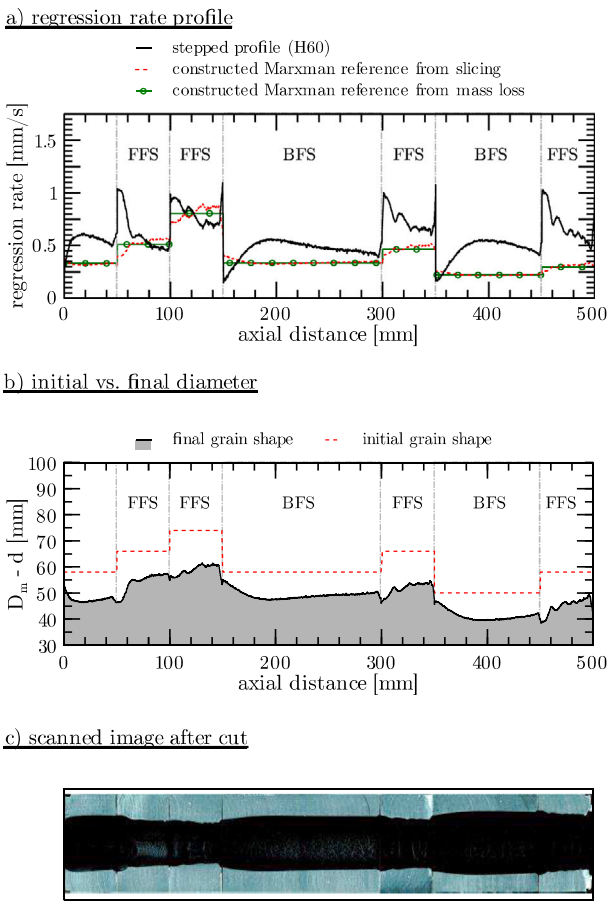


**Fig. 12.** H60 profiles (correct profile, coarse approximation).

H57, it can be noted that, overall, the shapes unique to BFS/FFS are still valid for all steps. Interestingly, for the FFS, the second peak of regression rate increase is almost measurable for the whole length of the FFS. This leads to the conclusion that the length-to-height ratio ($x/h$) of this profile is close to the optimum spacing. For H55 (alternating profile) the $x/h$ was around 7, in the present coarse profile it decreased now to 6, which seems to be almost the optimum. For the BFS cases, however, it is visible that the regression rate profiles for the first two BFS are not constant but decreasing. We predicted this effect numerically [8] already: BFSs need a certain height (numerically it was above 5 mm) to show a constant increase in regression rate for the remainder of the grain. Below this threshold, the regression rate profile resembles more an FFS, where a peak is visible that decreases further downstream. In Fig. 11(a), we can observe that the BFS regression profiles have a distant peak and then decrease with axial distance. This signifies that the step height for BFS (4 mm) for the inverted profile of H57 is too low to constantly increase the regression rate, contrary to the BFS in H55 (7.5 mm step height).

Having discussed the inverse profile of H57, we can now directly compare it with the correctly orientated coarse profile of H60. It is presented in Fig. 12. Firstly, the peaks of regression rate in Fig. 12(a) for the FFS parts are visible only over the first half of the step, proving that the length-to-height ratio is reduced compared to H57 (further away from the optimum). As for the BFS, the regression rate after the step is considerably higher than it was for the BFS cases in H57, showing that the height (8 mm vs. 4 mm) plays an important role for the BFS cases. Overall, the shapes and profiles of the steps are what were to be expected, judging from H55–H57. Therefore, the effect of steps in HREs can be predicted and anticipated because the regression rate profiles are reproducible throughout different mass flux levels and grain designs.

In the next section, we will investigate the impact of the grain orientation (inverse or correctly oriented) on the overall regression rate.

### 6.4. Time- and space averaged regression rates

In this section, we investigate the time- and space averaged regression rates to obtain information on the complete fuel grain throughout the burn. In Fig. 13, the temporal and spatial averaged regression rate is plotted. The average regression rate $\bar{\dot{r}}$ is estimated using the mass loss method (Section 3.2). With the points of the reference cases (H46–H49), the best fit for the Marxman law (without local dependency $x$) is plotted. Moreover, the tests with single steps of BFS (H52) and FFS (H50) are indicated from previous work [7,8]. The relative augmentation of regression rate for all cases to the reference curve are given in percent next to the data points.

The high value of the mass flux exponent $n = 1.328$ in Fig. 13 is to be noted. Typically, this exponent is found closer to 0.2–0.9 [21,41]. However, an exponent of 1.13 has been reported for the non-liquefiable fuels of Lengellé et al. [42] (as shown also in Ref. [41]) if the total mass flux $G$ is used instead of the oxidizer mass flux $G_{ox}$. When our exponent is calculated using $G$, the exponent $n$ reduces to 1.1 accordingly. Carmicino et al. [41] state the oxidizer injection as the primary driver of differing mass flux exponents. However, the approach to calculating the average mass flux (using the average port diameter or the average between the initial and final mass flux) has a significant impact on the exponent as well. For example, when our exponent is estimated with the initial and final total mass flux (instead of the average port diameter), the exponent reduces to $n = 0.95$. The true cause for the higher exponent in our cases is difficult to determine and part of

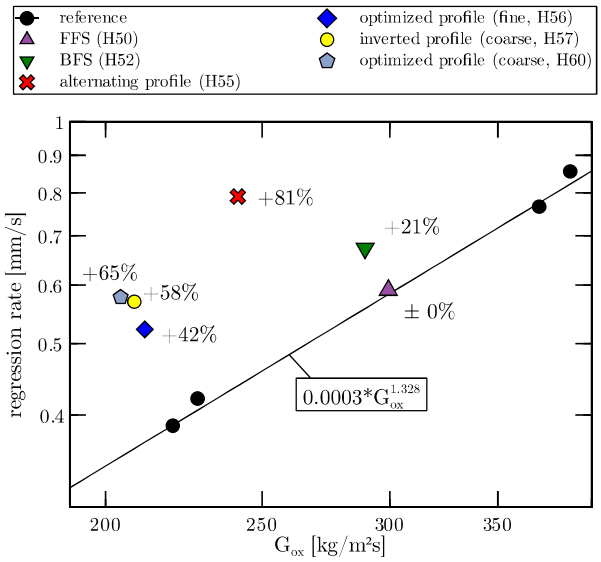


**Fig. 13.** Time- and space-averaged regression rates.

future investigations. Nonetheless, following the recommendation of Ref. [40], the average mass flux is calculated with the average fuel port diameter using Eq. (15).

Looking at Fig. 13, it is visible that a single FFS (H50) cannot increase the regression rate noticeably over the total fuel grain because the zone of higher regression rates is too short to have an impact on the total fuel grain length. On the other hand, a single BFS (H52) increases the regression rate by 21% because the regression rate after the step is increased at a constant level over the remainder of the fuel grain [7]. Based on these observations, the alternating fuel grain (H55) was created with 7 steps in total (4 BFS and 3 FFS). The total regression rate increase amounts to 81% on average for the total burn duration. Recalling the regression rate profiles of the alternating profile in Section 6.1, it became obvious that the effect of steps can be accumulated by deploying multiple steps (similar to what has been reported by Sakashi et al. [26] and Kumar and Joshi [27]). With H55, we also created a multi-stepped baseline, which allows us to assess the effect of the distribution on the average regression rate for tests H56 (fine profile), H57 (inverted coarse profile) and H60 (correct coarse profile).

Looking at H56, the regression rate increase dropped to 42% although more steps (10 in total, 7 FFS and 3 BFS) are used. The reason for this behavior is three-fold: first, more FFS than BFS are used. Based on our lessons learned, FFS are less performing than BFS, considering only the regression rate augmentation. Therefore, a slight drop in total regression rate increase was to be expected. Moreover, to have a fine approximation of the profile (recall Fig. 6), the step height was significantly reduced to 2 mm for FFS and 4 mm for BFS. Compared to the 7.5 mm of H55, it appears that the height of the step has a driving effect on the total regression rate increase. Finally, considering the final profile of the cut fuel grain in Fig. 9 for H56, we observed that the steps vanished during our burn time due to their smaller sizes. This signifies that the effects of the steps were also vanishing over time, thus, leading to a lower total regression rate augmentation.

Turning our attention to H57 (inverted coarse profile), it is to be reminded that during the preparations of the tests we accidentally mounted the fuel grain in a wrong orientation, leading to an inverted profile, which is exactly contradictory to what we wanted to achieve. The grain has now few but tall FFS and small but many BFS. Nonetheless, this allows us to test our postulation. The inverted profile consists of 4 BFS (4 mm height) and 2 FFS with 8 mm height. The total regression rate increase for H57 re-gained some percentages, up to 58%. The main reason for this increase is that the height of the steps in H57 was doubled compared to H56. Interestingly, although the profile is inverted (thus not following our rule of thumb for distribution of the steps), the regression rate of H57 is considerably higher than that of H56 where we respected the distribution rule. This leads to the important conclusion that the positioning of the steps based on the type (FFS vs. BFS) is less important than the relative height of the steps, if the steps are too small to sustain the total burn time. However, compared to the alternating profile of H55 where the tall steps (7.5 mm) are spaced according to our heuristic distribution rule, the regression rate of H57 (58%) is still below the 81% of H55. This underlines that the distribution of steps (while being less important than the total step height) still plays an important role. Therefore, the information we gained from re-testing the coarse profile in H60 is important.

In H60, the grain is inserted in the correct orientation, therefore following the rule of thumb of the distribution. The average regression rate increased from 58% (H57) to 65% (H60) although apart from the orientation of the grain the other experimental parameters were held the same. With this, we can prove that the distribution of steps according to our rule of thumb has a non-negligible effect on the regression rate increase.

We can formulate a novel heuristic model for the effect and distribution of steps in hybrids:

1. The step height has the most prominent effect on the regression rate. The higher the step (for both FFS and BFS), the higher the regression rate increase. Numerically [8], saturating behavior was noticeable above 10 mm for BFS and 5 mm for FFS.
2. BFSs increase the regression rate more than FFS for the grains in our motor (500 mm grain length). Only for very short grain lengths (110 mm) the FFS is more powerful [7].
3. When the steps are at approximately the same height, the steps need to be distributed accordingly (BFS sparsely distributed while FFS should be closer to each other) as has been visible in the higher regression rate of H60 compared to H57.
4. The approximation of profiles forces the step heights and distributions. If only the regression rate needs to be maximized for a certain grain above 110 mm, we postulate that using only BFS would yield the highest result. This is why H55 has the highest regression rate: H55 consists of 4 tall BFS, which is the highest number of all profiles.

An important aspect to be addressed when discussing the time-and space averaged regression rates is the vanishing of the steps over time. It has been observed for all multi-step grains, but most notably for the small step case H56 (Fig. 9). The experimental data strongly suggests that the steps and, consequently, the regression rate enhancing effect decreases over time. For future research, it is important to test the same profile over different time durations (e.g., 5 s, 10 s and 20 s) to evaluate the average regression rate increase at each time instance. In Fig. 13, all tests are conducted for the same burn duration, thus, the average regression rate of the cases is comparable. Nonetheless, for the future, detailed investigations into the impact of the burn duration need to be carried out.

## 7. Conclusion

In this work, we investigated the interaction of steps on the regression rate profiles of multi-step grains. Additionally, a genetic algorithm allows obtaining empirical Marxman parameters (even for the spatial resolution $x$) using only a single test instead of a combination of reference tests, which considerably decreases the experimental effort.

A total of three different fuel grain profiles were created: (a) an alternating profile with 3 forward facing steps and 4 backward facing steps of 7.5 mm height, (b) a more complex profile where the fuel port is approximated closely by 10 steps of 2–4 mm height, (c) the

same profile that is approximated coarsely by 6 steps (4–8 mm). Profile (c) was tested twice, once in inverted orientation and in the correct orientation.

The tests of the grains (a)– (c) were conducted on the HYCAT engine and the local regression rate profiles as well as the time- and space-averaged regression rates assessed. The following observations are to be noted:

1. The characteristic shape of the regression rate profile for each step type (forward vs. backward) was almost identical for all tests, proving that the mechanisms behind the regression rate increase are the same for different step heights (from 2 mm to 8 mm), step distributions and mass-flux levels.
2. The shapes of the regression rate are identical to previous experimental results of single steps. Multiple steps do not interfere negatively, and the regression rate enhancing effect of single steps can be accumulated.
3. In the case of step heights between 2 mm and 4 mm, for our 10 s tests, the steps vanish and leave a smooth profile which is close to the initial profile that needed to be approximated. Indeed, the vanishing of steps over time, and, consequently, the attenuation of the regression rate enhancing effects need to be addressed in future work.
4. The step height has a more pronounced effect on the regression rate increase than the proper distribution of the steps. In other words, if only the regression rate needs to be increased to a maximum, it is more important to employ higher steps rather than distributing them according to their area of influence.
5. If certain profiles need to be approximated with steps, the profile dictates the distribution of the steps. In our cases, this leads to lower regression rate increases than a purely alternating profile (42–65% vs. 81%)
6. Since backwards facing steps are more powerful to increase the regression rate, a multi-step grain with only backward facing steps that are sparsely distributed is postulated to have the highest regression rate.
7. When grains with similar step heights are compared (such as for H57 and H60), the proper distribution (long backward facing steps and short forward facing steps) becomes important again. This is visible in the higher regression rate of H60 that respects the rule of thumb and H57 that does not follow the correct distribution.

To conclude, we have shown that multiple steps can increase the regression rate of hybrid engines considerably (up to 81%; we suspect the limit is not yet reached). The results of single steps from our previous studies can be translated to multi-step grains, which makes them predictable. The insight into the local regression rate profiles for different step-step interactions can enable the derivation of mathematical models to compliment the classical Marxman theory when using steps for the future. Moreover, concerns for increased pressure instabilities induced by steps in fuel grains need to be investigated and addressed.

We have laid the foundation of a method to approximate numerous combustion chamber designs (even helical fuel grains [11]) by a set of different fuel grain cylinders that are assembled; allowing to tailor the performance of hybrid rockets to a wide range of use-cases.

## Declaration of competing interest

The authors declare that they have no known competing financial interests or personal relationships that could have appeared to influence the work reported in this paper.

## Acknowledgments

The authors would like to thank the technical experts of ONERA for the support of the test campaigns.

## Funding

The project leading to this application has received funding from the European Union's Horizon 2020 research and innovation programme under the Marie Sklodowska-Curie grant agreement No 860956. It is part of the ASCenSIon project, an Innovative Training Network (ITN) to advance space access capabilities (https://ascension-itn.eu/).

## References

[1] N. Davydenko, R. Gollender, A. Gubertov, V. Mironov, N. Volkov, Hybrid rocket engines: The benefits and prospects, Aerosp. Sci. Technol. 11 (1) (2007) 55–60, http://dx.doi.org/10.1016/j.ast.2006.08.008.

[2] A. Okninski, On use of hybrid rocket propulsion for suborbital vehicles, Acta Astronaut. 145 (2018) 1–10, http://dx.doi.org/10.1016/j.actaastro.2018.01.027.

[3] A. Mazzetti, L. Merotto, G. Pinarello, Paraffin-based hybrid rocket engines applications: A review and a market perspective, Acta Astronaut. 126 (2016) 286–297, http://dx.doi.org/10.1016/j.actaastro.2016.04.036.

[4] K. Kuo, M. Chiaverini, Challenges of hybrid rocket propulsion in the 21st century, in: Fundamentals of Hybrid Rocket Combustion and Propulsion, American Institute of Aeronautics and Astronautics, Reston, Virginia, 2007, pp. 593–638, http://dx.doi.org/10.2514/5.9781600866876.0593.0638.

[5] A. Okninski, W. Kopacz, D. Kaniewski, K. Sobczak, Hybrid rocket propulsion technology for space transportation revisited - propellant solutions and challenges, FirePhysChem (2021) http://dx.doi.org/10.1016/j.fpc.2021.11.015.

[6] C. Glaser, J. Hijlkema, J. Anthoine, Bridging the technology gap: Strategies for hybrid rocket engines, Aerospace 10 (10) (2023) 901, http://dx.doi.org/10.3390/aerospace10100901, URL https://www.mdpi.com/2226-4310/10/10/901.

[7] C. Glaser, R. Gelain, A.E.M. Bertoldi, Q. Levard, J. Hijlkema, J.Y. Lestrade, P. Hendrick, J. Anthoine, Experimental regression rate profiles of stepped fuel grains in hybrid rocket engines, Acta Astronaut. 204 (2023) 186–198, http://dx.doi.org/10.1016/j.actaastro.2022.12.045.

[8] C. Glaser, J. Hijlkema, J.Y. Lestrade, J. Anthoine, Influences of steps in hybrid rocket engines: Simulation and validation on simplified geometries, Acta Astronaut. (2023) http://dx.doi.org/10.1016/j.actaastro.2023.03.037.

[9] J.C. Vogel, J.K. Eaton, Combined heat transfer and fluid dynamic measurements downstream of a backward-facing step, 1985.

[10] G. Naka, C. Carmicino, J. Messineo, K. Kitagawa, T. Shimada, Evaluation of radiative heat-transfer effect on Paraffin-wax regression rate in hybrid rocket, J. Propuls. Power 39 (2) (2023) 258–273, http://dx.doi.org/10.2514/1.B38728, URL https://arc.aiaa.org/doi/10.2514/1.B38728.

[11] C. Glaser, J. Hijlkema, J.-Y. Lestrade, J. Anthoine, The stepped Helix hybrid rocket engine, in: AIAA AVIATION 2023 Forum, American Institute of Aeronautics and Astronautics, 2023, http://dx.doi.org/10.2514/6.2023-4028, URL https://arc.aiaa.org/doi/abs/10.2514/6.2023-4028.

[12] G. Young, T.L. Connell, K. Fennell, S. Possehl, M. Baier, Examining port geometry/solid loading for additively manufactured fuels in hybrid rockets, J. Propuls. Power 37 (2) (2021) 305–313, http://dx.doi.org/10.2514/1.B38033, URL https://arc.aiaa.org/doi/10.2514/1.B38033.

[13] R. Gelain, A.E.D.M. Bertoldi, A. Hauw, P. Hendrick, 3D printing techniques for Paraffin-based fuel grains, Aerotecnica Missili Spazio 101 (3) (2022) 257–266, http://dx.doi.org/10.1007/s42496-022-00126-5.

[14] C. Oztan, V. Coverstone, Utilization of additive manufacturing in hybrid rocket technology: A review, Acta Astronaut. 180 (2021) 130–140, http://dx.doi.org/10.1016/j.actaastro.2020.11.024.

[15] C. Nguyen, J.C. Thomas, Performance of additively manufactured fuels for hybrid rockets, Aerospace 10 (6) (2023) 500, http://dx.doi.org/10.3390/aerospace10060500, URL https://www.mdpi.com/2226-4310/10/6/500.

[16] C. Glaser, J. Hijlkema, J.Y. Lestrade, J. Anthoine, Hybrid rocket engines optimized by multi-stepped design approach: Experimental investigation, in: The 34th International Symposium on Space Technology and Science, Kurume, Japan, 2023.

[17] D.E. Goldberg, J.H. Holland, Genetic algorithms and machine learning, Mach. Learn. 3 (2) (1988) 95–99, http://dx.doi.org/10.1023/A:1022602019183.

[18] J. Hijlkema, A presentation of a complete design cycle for optimised hybrid rocket motors, in: SpacePropulsion 2018, Seville, 2018.

[19] G. Marxman, M. Gilbert, Turbulent boundary layer combustion in the hybrid rocket, in: Symposium (International) on Combustion, vol. 9, (no. 1) Elsevier BV, 1963, pp. 371–383, http://dx.doi.org/10.1016/s0082-0784(63)80046-6.

[20] D. Pastrone, Approaches to low fuel regression rate in hybrid rocket engines, Int. J. Aerosp. Eng. 2012 (2012) http://dx.doi.org/10.1155/2012/649753.

[21] C. Glaser, J. Hijlkema, J. Anthoine, Evaluation of regression rate enhancing concepts and techniques for hybrid rocket engines, Aerotecnica Missili Spazio (2022) http://dx.doi.org/10.1007/s42496-022-00119-4.

[22] P.A.O.G. Korting, H.F.R. Schöyer, Y.M. Timnat, Advanced hybrid rocket motor experiments, Acta Astronaut. 15 (2) (1987) 97–104, http://dx.doi.org/10.1016/0094-5765(87)90009-9.

[23] L. Kamps, K. Sakurai, Y. Saito, H. Nagata, Comprehensive data reduction for N2O/HDPE hybrid rocket motor performance evaluation, Aerospace 6 (4) (2019) http://dx.doi.org/10.3390/aerospace6040045.

[24] J. Lee, S. Rhee, J. Kim, H. Moon, Combustion instability mechanism in hybrid rocket motors with diaphragm, J. Propuls. Power (2021) 1–10, http://dx.doi.org/10.2514/1.B38492.

[25] O. Musa, G. Huang, Z. Yu, Effects of new solid propellant configurations on the combustion characteristics of a ramjet, Aerosp. Sci. Technol. 119 (2021) 107192, http://dx.doi.org/10.1016/j.ast.2021.107192.

[26] H. Sakashi, Y. Saburo, H. Kousuke, S. Takashi, Effectiveness of concave-convex surface grain for hybrid rocket combustion, in: 48th AIAA/ ASME/ SAE/ ASEE Joint Propulsion Conference and Exhibit, 2012, http://dx.doi.org/10.2514/6.2012-4107.

[27] M. Kumar, P. Joshi, Regression rate study of cylindrical stepped fuel grain of hybrid rocket, Mater. Today: Proc. 4 (8) (2017) 8208–8218, http://dx.doi.org/10.1016/j.matpr.2017.07.163.

[28] A. Gany, Y. Timnat, Parametric study of a hybrid rocket motor, Israel J. Technol. 10 (1972) 85–96.

[29] M. Grosse, Effect of a diaphragm on performance and fuel regression of a laboratory scale hybrid rocket motor using nitrous oxide and Paraffin, in: 45th AIAA/ASME/SAE/ASEE Joint Propulsion Conference and Exhibit, American Institute of Aeronautics and Astronautics, Reston, Virginia, 2009, http://dx.doi.org/10.2514/6.2009-5113.

[30] N. Bellomo, M. Lazzarin, F. Barato, A. Bettella, D. Pavarin, M. Grosse, Investigation of effect of diaphragms on the efficiency of hybrid rockets, J. Propuls. Power 30 (1) (2014) 175–185, http://dx.doi.org/10.2514/1.b34908.

[31] S. Zhang, F. Hu, D. Wang, P. Okolo.N, W. Zhang, Numerical simulations on unsteady operation processes of N2O/HTPB hybrid rocket motor with/without diaphragm, Acta Astronaut. 136 (2017) 115–124, http://dx.doi.org/10.1016/j.actaastro.2017.03.005.

[32] C.P. Kumar, A. Kumar, Effect of diaphragms on regression rate in hybrid rocket motors, J. Propuls. Power 29 (3) (2013) 559–572, http://dx.doi.org/10.2514/1.b34671.

[33] M. Dinesh, R. Kumar, Utility of multiprotrusion as the performance enhancer in hybrid rocket motor, J. Propuls. Power 35 (5) (2019) 1005–1017, http://dx.doi.org/10.2514/1.B37491.

[34] J.-Y. Lestrade, J. Anthoine, O. Verberne, A.J. Boiron, G. Khimeche, C. Figus, Experimental demonstration of the vacuum specific impulse of a hybrid rocket engine, J. Spacecr. Rockets 54 (1) (2017) 101–108, http://dx.doi.org/10.2514/1.a33467.

[35] A. Karabeyoglu, G. Zilliac, B.J. Cantwell, S. DeZilwa, P. Castellucci, Scale-up tests of high regression rate Paraffin-based hybrid rocket fuels, J. Propuls. Power 20 (6) (2004) 1037–1045, http://dx.doi.org/10.2514/1.3340.

[36] J. Schindelin, I. Arganda-Carreras, E. Frise, V. Kaynig, M. Longair, T. Pietzsch, S. Preibisch, C. Rueden, S. Saalfeld, B. Schmid, J.-Y. Tinevez, D.J. White, V. Hartenstein, K. Eliceiri, P. Tomancak, A. Cardona, Fiji: An open-source platform for biological-image analysis, Nature Methods 9 (7) (2012) 676–682, http://dx.doi.org/10.1038/nmeth.2019.

[37] C. Carmicino, A.R. Sorge, Influence of a conical axial injector on hybrid rocket performance, J. Propuls. Power 22 (5) (2006) 984–995, http://dx.doi.org/10.2514/1.19528.

[38] J.-E. Durand, J.-Y. Lestrade, J. Anthoine, Restitution methodology for space and time dependent solid-fuel port diameter evolution in hybrid rocket engines, Aerosp. Sci. Technol. 110 (2021) 106497, http://dx.doi.org/10.1016/j.ast.2021.106497.

[39] E. Quero Granado, G. Pelenghi, J. Hijlkema, J.-Y. Lestrade, J. Anthoine, A new system design tool for a hybrid rocket engine application, in: 73rd International Astronautical Congress, 2022.

[40] M.A. Karabeyoglu, B.J. Cantwell, G. Zilliac, Development of scalable space-time averaged regression rate expressions for hybrid rockets, J. Propuls. Power 23 (4) (2007) 737–747, http://dx.doi.org/10.2514/1.19226.

[41] C. Carmicino, A.R. Sorge, Role of injection in hybrid rockets regression rate behaviour, J. Propuls. Power 21 (4) (2005) 606–612, http://dx.doi.org/10.2514/1.9945.

[42] G. Lengelle, B. Fourest, J. Godon, C. Guin, Condensed-phase behavior and ablation rate of fuels for hybrid propulsion, in: 29th Joint Propulsion Conference and Exhibit, American Institute of Aeronautics and Astronautics, 1993, http://dx.doi.org/10.2514/6.1993-2413.